# Understanding the Extratropical Liquid Water Path Feedback in Mixed-Phase Clouds with an Idealized Global Climate Model

Michelle E. Frazer*

*Program in Atmospheric and Oceanic Sciences, Princeton University, Princeton, New Jersey*

Yi Ming

*NOAA/Geophysical Fluid Dynamics Laboratory, Princeton, New Jersey*

*Corresponding author*: Michelle E. Frazer, mefrazer@princeton.edu

## ABSTRACT

A negative shortwave cloud feedback associated with higher extratropical liquid water content in mixed-phase clouds is a common feature of global warming simulations, and multiple mechanisms have been hypothesized. A set of process-level experiments performed with an idealized global climate model show that the common picture of the liquid water path (LWP) feedback in mixed-phase clouds being controlled by the amount of ice susceptible to phase change is not robust. Dynamic condensate processes—rather than static phase partitioning—directly change with warming, with varied impacts on liquid and ice amounts. Here, three principal mechanisms are responsible for the LWP response, namely higher adiabatic cloud water content, weaker liquid-to-ice conversion through the Bergeron-Findeisen process, and faster melting of ice and snow to rain. Only melting is accompanied by a substantial loss of ice, while the adiabatic cloud water content increase gives rise to a net increase in ice water path (IWP) such that total cloud water also increases without an accompanying decrease in precipitation efficiency. Perturbed parameter experiments with a wide range of climatological LWP and IWP demonstrate a strong dependence of the LWP feedback on the climatological LWP and independence from the climatological IWP and supercooled liquid fraction. This idealized setup allows for a clean isolation of mechanisms and paints a more nuanced picture of the extratropical mixed-phase cloud water feedback than simple phase change.

## 1. Introduction

With atmospheric warming from greenhouse gases, cloud properties would vary in manifold ways, resulting in further changes in radiative fluxes and climate. Despite the recent advances in mechanistic understanding, the so-called cloud feedback is widely considered to be the largest contributor to the uncertainties in climate sensitivity and model projection of future warming (Sherwood et al. 2020). Ceppi et al. (2017) identifies three robust components of cloud feedback in comprehensive global climate models (GCMs): a positive longwave feedback from rising free tropospheric clouds, a positive shortwave (SW) feedback from decreasing subtropical low cloud fraction, and a negative SW feedback from increasing extratropical cloud optical depth.

Uncertainty associated with cloud feedback is dominated by the SW components (Soden and Vecchi 2011; Vial et al. 2013). Among these, this study focuses on the component that affects radiation through altering cloud optical depth or brightness (as opposed to cloud fraction). This cloud optical depth feedback is robustly negative in the Coupled Model Intercomparison Project Phase 5 (CMIP5) GCMs (Zelinka et al. 2016), though it may be artificially tuned to a small range (McCoy et al. 2016), and mechanistic uncertainty still abounds (Gettelman and Sherwood 2016; Ceppi et al. 2017; Korolev et al. 2017). Observations have shown that in pure liquid and mixed-phase (liquid and ice co-existing) clouds, cloud optical depth is primarily controlled by liquid water path (LWP), which is the vertically integrated cloud liquid (Stephens 1978). Ice affects cloud optical depth to a lesser extent owing to larger sizes of ice particles and ice water path (IWP) being generally smaller than LWP (Pruppacher and Klett 2010; McCoy et al. 2014; Cesana and Storelvmo 2017). GCMs predict a robust extratropical LWP increase in response to global warming, which is thought be the main driver of the negative SW cloud feedback (e.g. Ceppi et al. 2016).

Recent modeling studies have highlighted the need to improve GCM representation of the extratropical cloud feedback. Zelinka et al. (2020) showed that the increased climate sensitivity in CMIP6 models relative to CMIP5 is largely due to changes in this feedback. The multi-model ensemble mean changes from negative in CMIP5 to slightly positive in CMIP6 presumably due to model physics differences. Therefore, it is critical to delineate the underlying mechanisms of the extratropical cloud feedback and its various components.

Multiple pathways have been proposed to explain the extratropical increase (Ceppi et al. 2017) in liquid cloud condensate. The first is an increase in the adiabatic cloud water content. With warming, the amount of water condensed in saturated updrafts increases (Tselioudis et al. 1992; Gordon and Klein 2014); the fractional change is greater at colder temperatures (Betts and Harshvardhan 1987; Somerville and Remer 1984). The second mechanism involves phase change in mixed-phase clouds (e.g., Mitchell et al. 1989; Senior and Mitchell 1993; McCoy et al. 2015; Storelvmo et al. 2015; Tan et al. 2018), which occurs only at temperatures below freezing. As isotherms shift upward with warming, the liquid-to-ice ratio at a given mixed-phase cloud location is likely to increase (Tan et al. 2016), thereby increasing cloud optical depth. An implication of this phase change mechanism is that since liquid precipitates less efficiently than ice, total cloud water content may increase (Klein et al. 2009; McCoy et al. 2015; Ceppi et al. 2016; McCoy et al. 2018). This work will address both mechanisms and their impacts on LWP and IWP. A third potential mechanism frequently mentioned in the literature is poleward jet shifts. As this effect is highly model dependent and unlikely to be dominant (Kay et al. 2014; Ceppi and Hartmann 2015; Wall and Hartmann 2015; Ceppi et al. 2016), it is not explored here.

The relative importance of the proposed mechanisms is still unclear. LWP itself is robustly linked to temperature in both models (Ceppi et al. 2016) and observations (Terai et al. 2019), hinting at the potential for emergent constraints on the negative SW cloud feedback. McCoy et al. (2016) noted

that among CMIP5 GCMs, T5050, the diagnosed temperature at which liquid and ice exists in equal amounts globally, is strongly anti-correlated with LWP, but positively correlated with cloud fraction despite the lack of a physical explanation. At the same time, the range of T5050 (as well as a similarly-defined 90% glaciated temperature) estimated from space-borne observations is much lower than that diagnosed from CMIP5 models, suggesting that the models tend to freeze liquid at temperatures that are too high (Cesana et al. 2015; McCoy et al. 2016). Multiple GCM studies (McCoy et al. 2014; Tan et al. 2016; Frey and Kay 2018) have shown that increasing the ratio of supercooled liquid to total water (the so-called supercooled liquid fraction or SLF) in mixed-phase clouds decreases the SW negative feedback, and thus increases climate sensitivity. These results have been attributed to models with higher T5050 having more susceptible ice (McCoy et al. 2018), which is hypothesized to control the feedback strength (as in Tan et al. 2018). Improvements in understanding the governing mechanisms are especially important as some modeling studies with observationally-based constraints have suggested that the negative SW cloud optical depth feedback is too strong or even of the wrong sign in GCMs, implying that the actual climate sensitivity may be underestimated (e.g. Tan et al. 2016; Terai et al. 2016).

This work utilizes an idealized model to probe the physical mechanisms underlying the extratropical cloud water feedback. Idealized models complement comprehensive GCMs (Held 2005, 2014) since their workings are relatively easy to understand (Pierrehumbert et al. 2007). This is particularly true as previous studies of mixed-phase clouds are hindered by the non-linear complexity of cloud microphysics and the potential for unrealistic interactions between different parameterized processes (Ceppi et al. 2017). We seek to test the plausibility of the leading hypotheses in the mixed-phase cloud feedback literature including the simple conceptual picture of liquid increasing at the expense of ice with warming, which has fueled the notion of the extratropical LWP feedback being controlled by the amount of susceptible ice. As mentioned above, more ice in the control cli-

mate is thought to cause a greater increase in liquid with warming. The main supporting evidence is the positive correlation between the LWP feedback and climatological SLF or T5050 (McCoy et al. 2018; Tan et al. 2018). With a set of targeted, process-level experiments, we seek to explore the complexity of the mixed-phase cloud feedback. We also use a perturbed parameter ensemble of experiments with varied cloud physics settings to investigate the feasibility of predicting the LWP feedback from the control climate.

This paper is arranged as follows. Section 2 outlines the methodology. Section 3 presents the results from process-level and perturbed parameter experiments. Section 4 compares with previous studies with the goal of examining the plausibility of the phase change mechanism and other related arguments. Section 5 concludes as to rethinking the physical picture of the extratropical mixed-phase cloud feedback and suggests a path for future research.

## 2. Methodology

The idealized GCM used here combines a simple dry GCM with passive water and clouds as described in detail in Ming and Held (2018). The core is Held-Suarez dry dynamics (Held and Suarez 1994) at a T42 horizontal resolution (about 2.8° spacing) with 20 equally spaced vertical layers. Passive water vapor and cloud tracers (specific humidity, cloud liquid mixing ratio, cloud ice mixing ratio, and cloud fraction) are included, but are not allowed to feedback on the dynamics (i.e., no latent heating or cloud radiative effects). The cloud tracers evolve following a prognostic large-scale cloud scheme with bulk single-moment microphysics. The sub-grid-scale total-water-based relative humidity (RH) is assumed to follow a beta distribution, which is a function of the grid-mean RH. The beta distribution is designed such that a grid box with a mean total-water-based RH value above a certain threshold value ($RH_c$, 83.3% at the default half-width of 0.2) would have sub-grid-scale RH over 100%, thus producing clouds. The role of surface evaporation to

create the water vapor tracer is mimicked by nudging air parcels below 850 hPa toward saturation as in Galewsky et al. (2005). As clouds are completely decoupled from dynamics, this model a unique tool for isolating individual mechanisms in a clean fashion without circular feedbacks. With no convective parameterization, the application of the cloud scheme is limited to stratiform clouds (and not any mixed-phase clouds formed in shallow convection). Yet, as noted in Ming and Held (2018), while idealized, this model provides strong representation of cloud distribution in the extratropical free troposphere. The control simulation (Ctrl) is the model's default climate. For Ctrl and all perturbation experiments, the atmospheric state (e.g., temperature and winds) is identical at every time step. All model simulations include a 300-day spin-up, and the next 1000 days are averaged for analysis.

The bulk microphysics scheme has separate but interconnected treatments of liquid and ice based on Rotstayn (1997) and Rotstayn et al. (2000). The same scheme is also used in the GFDL AM2.1 model, one of the two models compared in Ceppi et al. (2016). As shown in Fig. 1, water vapor forms cloud liquid and ice through condensation and deposition, respectively. The initial partitioning of cloud liquid and ice is based entirely on temperature. All condensate at temperatures greater than -40°C is formed as liquid based on the consideration that ice nuclei are generally limited in the atmosphere (Rotstayn et al. 2000). Supercooled liquid (existing between 0° and -40°C) can then be converted to ice principally through the Bergeron-Findeisen (BF) process (and without an explicit treatment of heterogeneous ice nucleation). In the control climate, the primary sink of water vapor (98.8% globally) is conversion to cloud liquid. Microphysical sources of water vapor come from cloud liquid (evaporation), cloud ice (ice sublimation), rain (rain evaporation), and snow (snow sublimation). Together, rain evaporation and snow sublimation, the most significant microphysical sources, comprise 22.3% of all water vapor sources. Surface evaporation (a non-microphysical source) constitutes the main supplier of water vapor (76.4%).

Cloud liquid forms rain through autoconversion and accretion. To facilitate conversion of cloud liquid to ice through the BF process, a minimum amount of ice crystal mass ($10^{-12}$ kg) on which deposition can occur is assumed to be always present. (Note that the BF process is not formulated to be explicitly linked to aerosols.) Cloud liquid is also converted to cloud ice through riming (accretion of cloud liquid by ice) and homogeneous freezing (colder than -40°C). Overall, 68.2% of cloud liquid sinks are to rain and 30.9% to cloud ice. Cloud ice is lost almost completely (98.3%) to snow through ice settling. In the microphysics scheme, cloud ice and snow are treated effectively as one species, experiencing the same fall rate, and are only distinguished by their location in or outside of a cloud. Ice and snow can melt into rain: if this takes place in a cloud, it is considered melting of ice; if it takes places outside of a cloud, it is considered melting of snow. Cloud ice is also lost to water vapor through sublimation.

The *process-level experiments* involve increasing the temperature field fed to certain parts of the microphysics scheme or the formulation of surface evaporation by 2 K (summarized in Table 1). These isolated warming experiments are designed after Ceppi et al. (2016). Here, in the microphysics scheme (same as that used in the AM2.1 aquaplanet in Ceppi et al. (2016)), there are at least four explicitly temperature-dependent processes: partitioning of newly formed cloud condensate, the BF process, homogeneous freezing, and melting of ice and snow. When water vapor experiences condensation/sublimation at the beginning of the microphysics scheme, it is initially partitioned into cloud liquid and ice based solely on temperature. Only liquid is created at temperatures warmer than -40°C, and only ice otherwise. Supercooled liquid can be converted to ice through the BF process, homogeneous freezing, and riming. For the BF process, temperature affects whether or not the process occurs (below 0°C) as well as the rate of cloud liquid being converted to cloud ice, which is greater at lower temperatures (see Eqn. A8). These two effects are tested in combination (BF2K, subjecting the *BF* process to a *2-K* warming). (By contrast, riming

is not directly dependent on temperature; see Eqn. A10.) Homogeneous freezing of cloud liquid to ice occurs only when the temperature is less than -40°C and converts all cloud liquid to ice. Ice and snow melt into rain only when the temperature is higher than 0°C, with the melting being limited to the amount that would restore the grid-box temperature to 0°C. Melting of ice and snow are tested in combination (ME2K, subjecting *me*lting to a *2-K* warming). All of these microphysical processes—initial partitioning, the BF process, homogeneous freezing, and melting—are also perturbed in tandem in MI2K (*2-K* warming of *mi*crophysics).

A significant influence of temperature in the cloud scheme is in the calculation of the saturation specific humidity ($q_s$) and related variables (the $T$ derivative of $q_s$, the psychrometric constant, and the sum of the vapor diffusion and thermal conductivity factors) that are used in many parts of the scheme. Since surface evaporation is also formulated in parallel based on $q_s$, $q_s$ for microphysics and surface evaporation are perturbed simultaneously in Qse2K (*2-K* warming of $q_s$ for the *s*tratiform cloud scheme and *e*vaporation). This experiment enables us to study the effect of the adiabatic cloud water content increase. Finally, to cover all the aforementioned effects of temperature as well as any other effects (such as the influence of temperature on air density), a 2-K temperature increase is fed to the cloud scheme and surface evaporation to create the Tse2K (full warming) experiment.

To develop a predictive theory of the extratropical mixed-phase cloud feedback that is applicable to a wide range of control states, a set of *perturbed parameter experiments* (also summarized in Table 1) are created by systematically modifying three key parameters of the cloud scheme. The first two have been suggested as significant for the mixed-phase cloud feedback: the strength of the BF process may be too efficient (Tan et al. 2016) and $RH_c$ too high (McCoy et al. 2016). To vary the strength of the BF process, the formula for the conversion rate is altered arbitrarily by multiplying with a constant (0.25, 0.5, 2 or 4). The corresponding experiments are labeled as

quarBF, halvBF, doubBF and quadBF. Note that these adjustments do not result in actual changes in the BF rate as large as those imposed. The effective $RH_c$ (83.3% in Ctrl) is varied from 76.7% to 90.0% at increments of ~3.3% (rh767, rh800, rh867, and rh900) by altering the half-width of the sub-grid-scale RH beta distribution. Finally, a third parameter is chosen to cleanly affect the mean-state amount of cloud ice: the fall speed of cloud ice (relative to the large-scale vertical motion) is perturbed by multiplying with a constant (0.5, 0.75, 1.25 or 1.5). The corresponding experiments are v050, v075, v125 and v150. For each of these states, a Tse2K simulation (increasing the temperature field fed to the cloud scheme and surface evaporation by 2 K) is created, and the response (for example, rh767_Tse2K minus rh767) analyzed.

The key to understanding the steady-state mixing ratios of cloud liquid and ice ($q_l$ and $q_i$, respectively) and their responses to the warming is how they are related to the time tendencies of the aforementioned microphysical processes. To illustrate the point, let us write the time derivative of a variable $q$ ($q_l$ or $q_i$) as:

$$\frac{dq}{dt} = s - aq^b, \tag{1}$$

where $s$ is the source term, and the sink term is parameterized as a power-law function of $q$ with $a$ and $b$ as constants. It follows that the fractional change of $q$ can be related to the fractional change of $s$ by:

$$\frac{\delta q}{q} = \frac{1}{b}\frac{\delta s}{s}. \tag{2}$$

The formulation and behavior of the autoconversion parameterization (Eqn. A1) are discussed in Golaz et al. (2011) (see their Equations 12-14). Although the rate is nominally proportional to $q_l^{7/3}$, it is effectively controlled by a numerical limiter (Eqn. A3), which tends to set $q_l$ at a critical value ($q_{crit}$) determined by a tunable threshold droplet radius ($r_{thresh}$) and droplet number concentrations ($N$). Since neither $r_{thresh}$ nor $N$ changes in this study, $q_l$ should be close to $q_{crit}$

when autoconversion is the dominant process. By contrast, accretion is proportional to $q_l$ and the flux of rain (Eqn. A4). The BF rate (Eqn. A8) is effectively independent of $q_l$, but conditionally proportional to $q_i^{1/3}$. Riming (Eqn. A10) is proportional to $q_l$ and the flux of settling ice, which is related to the fall speed and $q_i$. Similarly, ice settling (Eqn. A6) at a specific level is determined by the fall speed and vertical gradient of $q_i$ ($\partial q_i / \partial p$, where $p$ denotes pressure). If $q_i$ is altered by the same ratio throughout the column, an assumption that holds approximately for the simulations examined here, the fractional change in the ice settling rate would be the same as that in $q_i$. The microphysical tendency equations are listed in the Appendix for reference. Condensation and deposition, the main sources of cloud liquid and ice, are not directly related to $q_l$ or $q_i$.

The analysis focuses on two variables: LWP and IWP, which are, respectively, vertically integrated cloud liquid and cloud ice in units of g $m^{-2}$. Absolute and fractional changes in LWP and IWP are normalized by warming and thus given in units of g $m^{-2}$ $K^{-1}$ and % $K^{-1}$, respectively. Due to the highly simplified nature of the boundary layer in this model (i.e., surface evaporation saturating the air below 850 hPa), for the purposes of this analysis the vertical integral has a lower boundary of 850 hPa such that LWP and IWP only represent the cloud condensate above 850 hPa. Similarly, specific humidity and cloud condensate tendency terms, when column-integrated, only represent values above 850 hPa. 30° to 60° and 60° to 90° are considered the mid-latitudes and high-latitudes, respectively, and together they are considered the extratropics. Data is averaged between the two hemispheres because of the hemispheric symmetry of the simulated climate. The supercooled liquid fraction (SLF) is calculated as the ratio of cloud liquid to total cloud water (liquid and ice). The daily SLF is binned as a function of temperature at an interval of 0.1 K for each grid box in the extratropical region above 850 hPa with the temperature at which SLF is closest to 50% considered to be T5050 (liquid and ice partitioned equally).

## 3. Results

### *a. Process-level Experiments*

Fig. 2 shows the zonal-mean LWP and IWP (averaged between hemispheres) in the control case (Ctrl), yielding a picture of the model's default climate [see Ming and Held (2018) for other related variables including RH and CF]. Here, LWP dominates IWP equatorward of the storm tracks (at around 45°); note that this LWP/IWP ratio is not directly comparable with full GCMs as here the boundary layer is excluded in the calculation of LWP and IWP. In the total warming experiment (Tse2K), the general features, including the location of the storm tracks, remain the same. Both LWP and IWP are higher at all latitudes in the warmer climate. The increase in LWP is more pronounced than that in IWP in the mid-latitudes, while they are more comparable in the high-latitudes.

Table 2 and Fig. 3 break down the LWP and IWP feedbacks seen in Tse2K. The increase in LWP (Fig. 3a) in the extratropics is dominated by the microphysical component (MI2K) with a much smaller (slightly less than 20%) contribution from the increased $q_s$ (Qse2K). MI2K and Qse2K combine nearly linearly to produce the full Tse2K increase in LWP suggesting that Tse2K does not add any significant temperature-affected processes beyond those perturbed in MI2K and Qse2K. The LWP feedback from the adiabatic water content increase is stronger in the high-latitudes (5.2% $K^{-1}$) than in the mid-latitudes (1.6% $K^{-1}$), as one would expect from the nonlinear temperature-dependence of the Clausius-Clapeyron relation.

Within the combined microphysical component, the BF process (BF2K) is responsible for most of the LWP increase, with a smaller contribution from melting (ME2K) present only in the mid-latitudes (Fig. 3b), and homogeneous freezing and initial phase partitioning producing negligible results (presumably because of the small amount of cloud condensate present near -40°C). The

BF effect is realized through the temperature-dependence of the conversion rate, as opposed to the temperature threshold at which the BF process takes control. LWP increases as the BF process slows down, converting less liquid to ice. The melting of snow to rain dominates the melting of ice to rain in terms of their effects in enhancing LWP. As discussed later, this can be conceptualized as a consequence of weaker riming since there is less snow (falling ice) to collect cloud liquid. Thus, we conclude that the increase in LWP with warming results primarily from a significant weakening of the BF process.

The IWP feedback is more nuanced. As shown in Fig. 3c, Qse2K and MI2K produce opposite effects: IWP increases at all latitudes in the former, while it decreases in the mid-latitudes with no significant change in the high-latitudes in the latter. In Qse2K, the normalized fractional increase in the high-latitude IWP (7.9% $K^{-1}$) is greater than the mid-latitude counterpart (6.7% $K^{-1}$), consistent with the adiabatic water content increasing with temperature at a faster rate at colder temperatures. The net result in Tse2K, to which Qse2K and MI2K add effectively linearly, is an increase in IWP, principally poleward of 45°. The relative importance of the BF process versus melting is reverse to the LWP feedback. The microphysical effect is dominated by ME2K (Fig. 3d); the enhanced melting of snow contributes to the lowering of IWP more than that of cloud ice. By contrast, BF2K gives rise to very little change in IWP. The fact that a weakening of the BF process causes a large increase in LWP, but no concurrent decrease in IWP is somewhat counter-intuitive, a point to which we will return later in this section when discussing the BF2K results in detail. (As with LWP, perturbing homogeneous freezing or initial phase partitioning produces no significant change in IWP.)

Fig. 4 shows the vertical structures of the changes in the mixing ratios of cloud liquid and ice. To better understand the underlying physical mechanisms, the main tendency terms driving the steady-state cloud liquid and ice are plotted in Figs. 5 and 6, respectively. No appreciable change

in $q_l$ is present below the freezing line in any experiment (Fig. 4) even when there are large local changes in cloud liquid tendencies, as is the case for condensation in Qse2K (Fig. 5a). It is also clear from Fig. 5 that autoconversion and accretion are the principal sinks of $q_l$ above 0°C in Ctrl, with autoconversion slightly stronger. As explained in Section 2, $q_{crit}$ exerts a strong control over $q_l$ when autoconversion dominates. By contrast, the BF process and riming take over in the mixed-phase cloud temperature range (between 0° and -40°C). Both the BF process and riming increase with the enhanced condensation in Qse2K (Fig. 5m and q). While the BF process is independent of $q_l$, since riming is proportional to $q_l$ steady-state $q_l$ increases (Fig. 4a). On the ice side, faster riming acts to increase $q_i$ (Fig. 6e). Moreover, the increased condensation leads directly to higher $q_i$ through the BF process (Fig. 6a), which is conditionally proportional to $q_i^{1/3}$. The resulting higher flux of settling ice, which is formulated to be approximately proportional to $q_i$, tends to further accelerate riming, but lower $q_l$. This cancels out much of the increase in $q_l$ caused by the increased condensation (Fig. 4a). The end result is that the normalized fractional increase in the extratropical IWP (6.8% $K^{-1}$) is much greater than the LWP counterpart (1.7% $K^{-1}$).

The imposed warming to the BF process (BF2K) slows down the BF conversion from liquid to ice (Fig. 5n). Since autoconversion and accretion play limited roles in the mixed-phase cloud regime, an acceleration of riming (Fig. 5r) is the only way to re-establish the $q_l$ tendency balance, causing a significant increase in $q_l$ (Fig. 4b). This re-balancing can be conceptualized as a weaker BF process producing more cloud liquid to be scavenged by falling ice through riming. Since the $q_l$ and $q_i$ tendencies (and their changes) are of the same magnitude but opposite signs for the BF process and riming, the effect of the two processes on $q_i$ is dictated by the balance of their $q_l$ counterparts (Fig. 6b and f). Because the effects of $q_i$ are of opposing sign, there is near-zero net change in cloud ice (Fig. 4f). This somewhat counterintuitive result emphasizes the need to evaluate changes in $q_l$ and $q_i$ based on process changes and a dynamic re-balancing of sources

and sinks. For example, when weakened BF process (as through warming) experiments were run with the riming process entirely removed from the microphysics scheme, instead of BF process $q_i$ tendency change being balanced principally by enhanced riming with little change in ice settling (as shown in Fig. 6f and j), without riming, the tendency change was principally balanced by significantly weakened ice settling.

The melting perturbation (ME2K) is unique in the sense that the resulting changes in cloud liquid and ice are of mirror image in terms of spatial structure (Fig. 4c and g). The main reason is that the melting perturbation effects are relatively confined to a narrow domain of a few degrees above the time-averaged freezing line. The warming-induced additional melting acts to increase the flux of rain and decrease the flux of settling ice simultaneously. Both factors have implications for $q_l$. The former tends to accelerate accretion with an effect of decreasing the $q_l$ tendency, while the latter acts to slow down riming which increases the $q_l$ tendency. The simulation shows a net increase of $q_l$, suggesting that the latter factor prevails over the former. The signs of the simulated rate changes are consistent with the expectations, and they largely balance out each other (Fig. 5k and s), with a weaker contribution from autoconversion (Fig. 5g). On the ice side, the reduced supply of ice from riming is balanced entirely by lowering $q_i$ and thus settling (Fig. 6g and k). The role of the BF process here is negligible as it is relatively ineffective at temperatures within a few degrees of 0 °C.

This process-level analysis illustrates why the principal components of the full warming (Tse2K) simulation, namely Qse2K, BF2K, and ME2K, increase $q_l$ and hence LWP, as summarized schematically in Fig. 7. Although they all point in the same direction, the microphysical warming components (BF2K and ME2K) are a stronger contribution to the LWP feedback than the macrophysical/thermodynamic component (Qse2K). The extratropical IWP feedback stems from a broad increase in $q_i$ from Qse2K being offset partially by a decrease near the freezing line from ME2K.

The results underscore that multiple processes with distinct characteristics are influential in shaping the LWP and IWP responses, and contradict the common picture suggested in mixed-phase cloud feedback literature of an effective trade-off between ice and liquid. Here, the dominant processes which increase LWP with warming in mixed-phase clouds are not doing so at the expense of ice, so the actual picture is more complicated than a (direct or indirect) conversion from ice to liquid with warming. Liquid and ice in mixed-phase clouds are not in a static equilibrium; rather, they exist in a dynamic balance of sources and sinks. These source and sink processes are directly changed by warming as opposed to a simple temperature-dependent phase partitioning.

*b. Perturbed Parameter Experiments*

To further explore the sensitivity of the LWP and IWP feedbacks, a set of alternative control states was created by altering three key aspects of the cloud scheme, namely the value of $RH_c$, the strength of the BF process and the fall speed of ice ($v_{fall}$, Eqn. A7), summarized in Table 1. As shown in Fig. 8, the first two changes produce a wide range of the climatological LWP (approximately a factor of 2), but little variation in IWP. Lower $RH_c$ or weaker BF process leads to higher LWP. While these experiments are not designed to fully explain the insensitivity of IWP to $RH_c$ or the BF process in more detail than the previous section, the broad principle is that steady-state values are determined by a dynamic balance of continuing phase conversion, not a static equilibrium. And, ice changes are harder to manufacture using local processes (like the BF process) when ice is so strongly controlled by gravitational settling. In the $v_{fall}$ perturbations, IWP varies widely (a factor of more than 3) with higher fall speed giving rise to lower IWP but with little spread in the climatological LWP.

All of these perturbed parameter experiments are subjected to 2-K warming in a way analogous to Tse2K. The resulting normalized LWP and IWP changes ($\delta$LWP and $\delta$IWP, respectively) are

plotted against their climatological counterparts in Fig. 9. Ranging from 2.6 to 3.4 g $m^{-2}$ $K^{-1}$, relative to 3.0 g $m^{-2}$ $K^{-1}$ in Tse2K (Table 2), the LWP feedback is positively correlated with the climatological LWP (Fig. 9a). The best linear fit yields that $\delta$LWP = 0.045 LWP + 1.60, with an $R^2$ of 0.98. Thus, the fractional change can be written as $\delta$LWP/LWP = 0.045 + 1.60/LWP, suggesting that the marginal gain decreases with increasing LWP. Since the four experiments targeting the BF process, namely {quar, halv, doub, quad}BF, effectively demonstrate the basic behavior of the LWP feedback, we start by focusing on them in the effort to explain the latter. As shown above, the main sink terms for cloud liquid in the mixed-phase regime are the BF process and riming. As the BF process becomes stronger from quarBF to quadBF, riming has to weaken if the total sink is constant, giving rise to lower climatological LWP, in line with the model simulations. Recall that the riming rate is proportional to cloud liquid. The process-level experiments suggest that the warming effect is realized mostly through the BF process. In these experiments, the warming-induced perturbation to the BF process is roughly proportional to its baseline rate (not shown). Therefore, the lower the climatological LWP is, the stronger the baseline BF rate and associated perturbation are. The combination translates into higher fractional change in LWP with lower climatological LWP (from a stronger BF process).

Lowering $RH_c$ tends to increase LWP by enhancing condensation in a way similar to Qse2K. They differ in that the former causes a large increase in autoconversion, but without any substantial change in accretion or riming, while all three processes increase in the latter. As explained before, autoconversion can adjust to forced changes such as those resulting from warming without perturbing cloud liquid. As a result, a control state with enhanced autoconversion should be less sensitive to warming (in this limited context; other feedbacks in complex models such as that noted in Mülmenstädt et al. (2021) may complicate this picture). This explains why lowering $RH_c$ gives rise to larger LWP, but smaller fractional increases in response to warming. Of interest is

the minimal effect on the extratropical climatological LWP and $\delta$LWP from drastically changing the climatological IWP (or susceptible ice) in the ice fall speed experiments. Clearly, the LWP feedback is correlated with the climatological LWP, but not the climatological IWP. The preceding analysis also holds when the LWP feedback is further divided into the mid- and high-latitude components (not shown).

The IWP feedback is correlated strongly with the climatological IWP (Fig. 9b). Note that the variation in the IWP feedback is almost exclusively from the ice fall speed experiments (ranging from 0.57 to 1.70 g $m^{-2}$ $K^{-1}$). An inspection of the best linear fit result ($\delta$IWP = 0.023·IWP + 0.031, with an $R^2$ of 1.00) indicates that the intercept is so small that the warming-induced change in IWP is effectively proportional to the climatological IWP. In other words, the normalized fractional change is constant at 2.3% $K^{-1}$. This relatively simple relation reflects the fact that gravitational settling is the main process through which cloud ice can be adjusted to re-establish the mass balance. As seen both from the process-level experiments and the BF-series parameter perturbation experiments, the amount of cloud ice is not sensitive to the BF process. In the meantime, riming is under the strong control of the cloud liquid balance. This leaves gravitational settling as the only way to alter cloud ice without affecting other processes substantially. Note that similar linear relationships hold if the climatological LWP and IWP are computed only for the mixed-phase temperature range (between 0 and -40°C), confirming the independence of the LWP feedback from the climatological IWP (or susceptible ice).

## 4. Discussion

As noted in the introduction, much of the existing literature on the extratropical mixed-phase cloud feedback centers on the correlation between the climatological SLF/T5050 and LWP feedback. Specifically, the lower SLF is or the higher T5050 is, the stronger the LWP feedback is (Tan et al.

2016; Frey and Kay 2018; McCoy et al. 2018). The presumption is that the phase change mechanism plays a crucial role, meaning that ice would be statistically replaced by liquid as isotherms shift with warming. Thus, the climatological susceptible ice or IWP is thought to be predictive of the feedback strength, forming the basis of potential emergent constraints (Tan et al. 2016). A related argument is that the phase change would give rise to a decrease in precipitation efficiency and a net increase in total water path (TWP, the sum of LWP and IWP) as liquid is less efficient than ice in forming precipitation (McCoy et al. 2018). While it is clear from the previous section that the mixed-phase cloud feedback is much more complicated than simple phase change, we further test the validity of both claims—SLF/T5050 as a predictor and decreased precipitation efficiency increasing TWP—against our results.

The climatological T5050 in the perturbed parameter experiments spans a wide range (~15 K) (Fig. 10). Stronger BF process and higher $RH_c$ favor lower LWP (or SLF) and higher T5050. The normalized $\delta$LWP, however, is strongly anti-correlated with T5050 ($R^2$ = 0.92, Fig. 10) as it is positively correlated with the climatological LWP (Fig. 9a). The T5050/$\delta$LWP anti-correlation is opposite to that expected if susceptible ice drove the LWP feedback and is contrary to the findings of Tan et al. (2016) and Frey and Kay (2018) based on the CAM5 model and of McCoy et al. (2018) based on CMIP5 models. Furthermore, as shown in Fig. 8, the climatological IWP is effectively constant for these experiments. This calls into question the hypothesis that susceptible ice controls the strength of the LWP feedback. As another evidence against the hypothesis, if the $v_{fall}$ perturbations are included, the predictive power of T5050 is significantly diminished ($R^2$ = 0.76, Fig. 10). The large variations in the climatological IWP, which drive the spread in T5050 in the $v_{fall}$ perturbations, do not affect $\delta$LWP significantly. Thus, any connection here between T5050 and the LWP feedback is not derived from the climatological ice but rather the climatological liquid. This finding suggests that it is important to, when showing correlation between changes in

T5050 (or SLF) and LWP feedback or climate sensitivity, also consider the independent roles of changes in climatological liquid or ice as potentially meaningful in addition to their ratio.

To understand why a T5050/LWP feedback connection might be present in some models but not others, we consider the dissection of mechanisms for LWP increase in aquaplanet versions of CAM5 and AM2.1 in Ceppi et al. (2016). AM2.1 uses virtually the same large-scale cloud parameterizations as our idealized model, and the AM2.1 results documented in Ceppi et al. (2016) are in excellent agreement with ours despite numerous differences in model setup and experimental design, a testament to the central role of cloud parameterizations in determining the feedback. Whereas both CAM5 and AM2.1 yield higher LWP in response to warming, their IWP changes differ in sign (see their Figure 2). IWP decreases in CAM5, but increases in AM2.1. Moreover, microphysical processes, especially the BF process, are responsible for the majority of the LWP increases, but cannot even account for the signs of the combined extratropical IWP changes (their Figure 7): the microphysically-induced IWP change is an increase in CAM5 and a decrease in AM2.1. Note that CAM5 implements the Morrison-Gettelman microphysics scheme (Morrison and Gettelman 2008), which differs significantly from the Rotstayn-Klein microphysics scheme (Rotstayn 1997) used in AM2.1 and our model, particularly in the treatment of ice and snow. As noted previously, the Rotstayn-Klein scheme treats cloud ice and snow indistinguishably and therefore lacks direct representation of cloud ice autoconversion and accretion by snow (though tuning of the ice fall speed can indirectly account for these sinks of cloud ice). Additionally, the Morrison-Gettelman scheme includes a representation of ice nucleation, which was found in Tan and Storelvmo (2016) to have an even stronger effect than ice fall speed on LWP and IWP. In this sense, it is not inconceivable to see microphysically-induced IWP changes being qualitatively different between the two models. Clearly, the large discrepancy in IWP response to warming merits

445 further analysis and evaluation of both microphysics schemes, especially given the important role
446 of ice cloud microphysics for Arctic cloud feedback (Tan and Storelvmo 2019).

447 Beyond the microphysical feedback, in the Ceppi et al. (2016) study, if one assumes linear
448 additivity (which appears to hold) the non-microphysical component of the IWP change would be
449 a net loss in CAM5 and a net gain in AM2.1. Our results demonstrate that the non-microphysical
450 enhancement of IWP in AM2.1 is attributable to the adiabatic cloud water content increase, a
451 possibility noted in Ceppi et al. (2016). Thus, attempting to reconcile this work with others raises
452 the intriguing question of what factors could outweigh the adiabatic cloud water content effect
453 (however strong it is) and cause the net loss seen in CAM5. These factors (perhaps related to
454 convective ice) should be further explored in complex GCMs and the adiabatic ice effect evaluated
455 for robustness. From the process dissection in Ceppi et al. (2016), it appears that the considerable
456 loss of cloud ice in the warming experiments conducted with CAM5 in Tan et al. (2016) and Frey
457 and Kay (2018) is not microphysical (stratiform) in origin, and thus should not be interpreted
458 as being related to the concurrent increase of cloud liquid, which roots in microphysics. This
459 mechanistic understanding casts further doubt on the susceptible ice hypothesis and other related
460 arguments. From a broader perspective, Ceppi et al. (2016) also noted a robust extratropical
461 LWP increase with warming in the CMIP5 model ensemble mean, without a compensating large
462 decrease in IWP. This is consistent with other studies showing diverse extratropical LWP and IWP
463 feedbacks in models beyond the two highlighted by Ceppi et al. (2016). For example, Lohmann
464 and Neubauer (2018), using ECHAM6-HAM2 with microphysics after Lohmann and Roeckner
465 (1996), found no increase in ECS with increased SLF (unlike the relation found in Tan et al. 2016).
466 McCoy et al. (2021) showed that among CMIP5 and CMIP6 GCMs, most show an increase in
467 liquid along with a slight reduction in ice.

Having seen no evidence of the utility of SLF/T5050 as a predictor here for LWP feedback, we now consider whether decreased precipitation efficiency contributes here to the increase in TWP. We calculate the large-scale precipitation efficiency as defined in Zhao (2014), which is the ratio of the total cloud condensation rate (the sum of condensation and deposition fluxes) to surface precipitation and represents the fraction of the condensate that subsequently rains out. There is a slight increase in precipitation efficiency with warming (80.5% in Ctrl versus 81.1% in Tse2K). This results from microphysical increases (80.7% in BF2K and 80.8% in ME2K) being offset by a macrophysical decrease (80.0% in Qse2K). All changes are on the order of 1% or less. Critically, no evidence of an increase in cloud lifetime is present, with precipitation efficiency increasing rather than decreasing. Another measure of a precipitation efficiency effect is surface precipitation normalized by TWP (P/TWP) as in McCoy et al. (2015), which can be thought of as the inverse of the cloud water residence time. Following the Clausius-Clapeyron relation, the extratropical surface precipitation increases by 6.9% $K^{-1}$ in Tse2K and Qse2K, but remains essentially constant in the microphysical experiments. P/TWP increases by 1.9% from 1.03 $hr^{-1}$ in Ctrl to 1.05 $hr^{-1}$ in Tse2K. Again, the net result is a slight decrease in the cloud water residence time or a slight increase in precipitation efficiency. These results do not support a precipitation efficiency effect with warming here as widely claimed (e.g., at the heart of the argument of Bjordal et al. 2020).

This finding does not mean a precipitation efficiency feedback is not present in reality, but it may not be present in models as assumed. Mülmenstädt et al. (2021) showed that when warm rain parameterizations are adjusted to better simulate reality in a complex GCM (ECHAM-HAMMOZ), a large negative cloud lifetime effect becomes present. Here we show that other mechanisms can explain a significant increase in LWP and TWP, emphasizing the need to carefully diagnose mechanisms to explain model results which may not contain a significant precipitation efficiency feedback without a warm rain efficiency adjustment. In our model, the weakening of the BF process

(BF2K) increases TWP while keeping precipitation nearly constant, suggesting that the BF process alone could affect precipitation efficiency, and thus should be the focus of research to improve its representation in models in addition to the need for improvement in warm rain efficiency as highlighted by Mülmenstädt et al. (2021)

Here, in the absence of a precipitation efficiency-mediated strong phase change effect, the adiabatic cloud water content effect is shown to be responsible for increasing TWP by enhancing both liquid and ice. McCoy et al. (2015) observed that increasing TWP was a significant contribution to increased extratropical LWP in CMIP5 models, with only 20−80% of the LWP increase being due to phase re-partitioning. Using observations and modeling, McCoy et al. (2019) highlighted the primacy of the adiabatic cloud water content effect in explaining the increase in LWP with warming in extratropical cyclones. It was found that more than 80% of the enhanced Southern Ocean extratropical cyclone LWP in GCMs from warming can be predicted based on the relationship between the climatological warm conveyor belt moisture flux and cyclone LWP and the change in moisture flux with warming (see also McCoy et al. 2020). While phase change may play a role in the remaining unexplained LWP increases, especially in the poleward half of cyclones, it is clearly a secondary mechanism. A ground-based observational study (Terai et al. 2019) found that both the moist adiabatic scaling and phase partitioning mechanisms are equally important for explaining the increase in LWP with warming at cold temperatures. A complementary space-based observational study (Tan et al. 2019), however, suggests phase change is more important than the adiabatic cloud water content increase in explaining the increase in cloud optical depth with cloud top temperature. Between these observational studies, the GCM studies referenced in this Discussion section, and the idealized modeling results presented herein, it is clear that more research is clearly needed for elucidating the relative importance of the two mechanisms. These mechanisms, as well as a

potential precipitation efficiency mediated effect, should be carefully diagnosed in future GCM research as an important step in constraining the mixed-phase cloud feedback.

## 5. Conclusions

This study used an idealized GCM to perform a set of process-level experiments which delineated three key mechanisms of the extratropical LWP feedback involving mixed-phase clouds: higher adiabatic cloud water content, weaker liquid-to-ice conversion through the BF process, and strengthened melting of ice and snow to rain with associated impacts on riming. Over half of the extratropical LWP increase can be attributed to the weakening of the BF process, without a corresponding decrease in IWP. The extratropical IWP in fact increases with warming due to the adiabatic cloud water effect, with a small offset caused by stronger melting. Warming experiments in a perturbed parameter ensemble demonstrate a strong dependence of the LWP feedback on the climatological LWP and independence from the climatological IWP. T5050 is anti-correlated with $\delta$LWP and is therefore only useful as a predictor insofar as it represents the climatological LWP as opposed to the climatological IWP. No associated decrease in precipitation efficiency is found in this modelling setup.

The overarching goal of this study is to improve mechanistic understanding of the extratropical mixed-phase cloud feedback. Our results help refine the current physical conceptualization of the LWP feedback as more nuanced than simple phase change, involving impacts of higher adiabatic cloud water content, weaker cloud liquid sinks such as the BF process, and indirect phase changes moderated by precipitation processes (especially riming). Liquid and ice in mixed-phase clouds are in a dynamic equilibrium with microphysical process efficiencies defining time-averaged phase partitioning and its change with warming. These results are helpful for guiding efforts to constrain mixed-phase parameterizations in GCMs through process-oriented diagnostics. In particular, the

effect of warming on the BF process, which is at the heart of mixed-phase cloud microphysics, should be better understood and represented in GCMs (see Tan and Storelvmo 2016). In addition to the BF process, the climatological LWP needs to be better constrained. Not only is it shown here to be predictive of the LWP feedback, but also the radiative impact of increases in LWP is highly dependent on the control state (Bodas-Salcedo et al. 2016, 2019). Finally, similar process-based studies, especially among varying microphysics schemes, are vital, as cloud water source and sink efficiencies define the mixed-phase cloud phase partitioning (Ceppi et al. 2016). Mixed-phase cloud studies should show results at the process level to better conclude as to the driving mechanisms and implications for climate sensitivity. Because of complex interactions in full GCMs when mixed-phase physics are perturbed (as in Tan et al. 2016; Frey and Kay 2018), idealized setups such as that utilized here present a clean, complementary approach for elucidating causal relationships.

*Acknowledgments.* The authors acknowledge Nadir Jeevanjee and David Paynter for helpful feedback and Daniel McCoy for useful discussion. M.E.F. was supported by award NA18OAR4320123 from the National Oceanic and Atmospheric Administration, U.S. Department of Commerce, and award AWD1005319 from the National Science Foundation.

*Data availability statement.* The output from the simulations described in this manuscript is archived at the Geophysical Fluid Dynamics Laboratory and is available upon request.

# APPENDIX

## Microphysical Transformation Equations

The following equations are those parameterized in the microphysical scheme used herein (after Rotstayn 1997; Rotstayn et al. 2000).

*a. Precipitation Formation Processes*

*Autoconversion*: the time rate change of grid mean liquid from autoconversion is parameterized as:

$$\left.\frac{\partial q_l}{\partial t}\right|_{au} = -q_a \times \left(\frac{0.104 g \rho^{4/3} E_{c,au}}{\mu (N\rho_l)^{1/3}}\right) \times (q_l/q_a)^{7/3} \times H(r_d - r_d^{au}) \tag{A1}$$

where $\mu$ is the dynamic viscosity of air, $E_{c,au}$ is the mean collection efficiency of the autoconversion process, $\rho_l$ is the density of pure liquid, and $N$ is the number of cloud droplets per unit volume. In the Heaviside function, $H$, $r_d^{au}$ is a critical drop radius that the mean volume radius of cloud drops, $r_d$, must exceed for autoconversion to occur, where:

$$\rho q_l/q_a = 4\pi N \rho_l r_d^3/3 \tag{A2}$$

Autoconversion is limited to that which would decrease $q_l$ to the threshold:

$$MAX\left(-\left.\frac{\partial q_l}{\partial t}\right|_{au}\right) = \ln\left(\frac{\rho q_l/q_a}{4\pi N \rho_l (r_d^{au})^3/3}\right) \times \frac{q_l}{\Delta t_{cld}} \tag{A3}$$

*Accretion*: the time rate change of grid mean liquid from accretion is parameterized as:

$$\left.\frac{\partial q_l}{\partial t}\right|_{acc} = -a_{rain}^{cld} \times 65.8 E_{c,acc} (R_{rain}^{cld}/\rho_l a_{rain}^{cld})^{7/9} \times (q_l/q_a) \tag{A4}$$

where $R_{rain}^{cld}$ is the grid mean flux of rain entering the rid box from above that enters saturated air, $a_{rain}^{cld}$ is the portion of the grid box that this occurs in, and $E_{c,acc}$ is the collection efficiency between rain drops and cloud droplets which is parameterized as:

$$E_{c,acc} = r_d^2/(r_d^2 + 20.5\mu^2) \tag{A5}$$

*Gravitational Settling*: the sink of cloud ice due to gravitation settling is:

$$\left.\frac{\partial q_i}{\partial t}\right|_{gr} = -\frac{\partial}{\partial p}\{q_a \times \rho g V_f \times (q_i/q_a)\} \tag{A6}$$

where $V_f$ is the fall speed the cloud ice fall as relative to the large-scale vertical motion and is parameterized as:

$$V_f = 3.29(\rho q_i/q_a)^{0.16} \tag{A7}$$

*b. Conversions between Liquid and Ice*

*BF Process*: the time rate change of the Bergeron-Findeisen process (growth of an ice crystal from preferential condensation) is parameterized as:

$$\left.\frac{\partial q_l}{\partial t}\right|_{berg} = -\frac{q_a \times (N_i/\rho)^{2/3} \times 7.8 \times (MAX(q_i/q_a, M_{i0}N_i/\rho))^{1/3}}{(\rho_i)^{2/3} \times (A+B)} \tag{A8}$$

where $N_i$ is the number of ice nuclei per unit volume, $M_{i0}$ is the mass ($10^{-12}$) of an initial crystal assumed to always be present, $\rho_i$ is the mass density of pristine ice crystals. Additionally, $A = (L_v/K_aT) \cdot ((L_v/R_vT) - 1)$ and $B = R_vT/\chi e_s$, where $K_a$ is the thermal conductivity of air, $\chi$ is the diffusivity of water vapor in air, and $R_v$ is the gas constant for water vapor. The ice nuclei density, $N_i$, is parameterized assuming the air is a liquid water saturation:

$$N_i = 1000 \exp\left[12.96\frac{(e_{sl} - e_{si})}{e_{si}} - 0.639\right] \tag{A9}$$

where $e_{sl}$ and $e_{si}$ are the saturation vapor pressures over liquid and ice, respectively.

*Riming*: the time rate change of riming (falling ice colliding and coalescing with cloud droplets) is parameterized as:

$$\left.\frac{\partial q_l}{\partial t}\right|_{rim} = -a^{cld}_{snow} \times \lambda_f E_{c,rim}(R^{cld}_{snow}/2\rho_i a^{cld}_{snow}) \times (q_l/q_a) \tag{A10}$$

where $\rho_i$ is the assumed density of falling ice crystals, $R^{cld}_{snow}$ is the grid mean flux of settling ice entering the rid box from above that enters saturated air, $a^{cld}_{snow}$ is the portion of the grid box that this occurs in, $E_{c,rim}$ is the collection efficiency for the riming process (fixed), and $\lambda_f$ is parameterized as a function of temperature:

$$\lambda_f = 1.6 \times 10^3 \cdot 10^{0.023(276.16K - T)} \tag{A11}$$

## References


Betts, A. K., and Harshvardhan, 1987: Thermodynamic constraint on the cloud liquid water feedback in climate models. *J. Geophys. Res.*, **92**, 8483–8485, doi:10.1029/JD092iD07p08483.

Bjordal, J., T. Storelvmo, K. Alterskjær, and T. Carlsen, 2020: Equilibrium climate sensitivity above 5$^o$C plausible due to state-dependent cloud feedback. *Nat. Geosci.*, **23**, 718–721, doi:10.1038/s41561-020-00649-1.

Bodas-Salcedo, A., P. G. Hill, K. Furtado, K. D. Williams, P. R. Field, J. C. Manners, P. Hyder, and S. Kato, 2016: Large contribution of supercooled liquid clouds to the solar radiation budget of the Southern Ocean. *J. Climate*, **29**, 4213–4228, doi:10.1175/JCLI-D-15-0564.1.

Bodas-Salcedo, A., J. P. Mulcahy, T. Andrews, K. D. Williams, M. A. Ringer, P. R. Field, and G. S. Elsaesser, 2019: Strong dependence of atmospheric feedbacks on mixed-phase microphysics and aerosol-cloud interactions in HadGEM3. *J. Adv. Model. Earth Syst.*, **11**, 1735–1758, doi:10.1029/2019MS001688.

Ceppi, P., F. Brient, M. D. Zelinka, and D. L. Hartmann, 2017: Cloud feedback mechanisms and their representation in global climate models. *WIREs Clim. Change*, **8**, doi:10.1002/wcc.465.

Ceppi, P., and D. L. Hartmann, 2015: Connections between clouds, radiation, and midlatitude dynamics: A review. *Curr. Clim. Change. Rep.*, **1**, 94–102, doi:10.1007/s40641-015-0010-x.

Ceppi, P., D. L. Hartmann, and M. J. Webb, 2016: Mechanisms of the negative shortwave cloud feedback in middle to high latitudes. *J. Climate*, **29**, 139–157, doi:10.1175/JCLI-D-15-0327.1.

Cesana, G., and T. Storelvmo, 2017: Improving climate projections by understanding how cloud phase affects radiation. *J. Geophys. Res. Atmos.*, **122**, 4594–4599, doi:10.1002/2017JD026927.

Cesana, G., D. E. Waliser, X. Jiang, and J. F. Li, 2015: Multimodel evaluation of cloud phase transition using satellite and reanalysis data. *J. Geophys. Res. Atmos.*, **120**, 7871–7892, doi:10.1002/2014JD022932.

Frey, W. R., and J. E. Kay, 2018: The influence of extratropical cloud phase and amount feedbacks on climate sensitivity. *Climate Dyn.*, **50**, 3097–3116, doi:10.1007/s00382-017-3796-5.

Galewsky, J., A. Sobel, and I. M. Held, 2005: Diagnosis of subtropical humidity dynamics using tracers of last saturation. *J. Atmos. Sci.*, **62**, 3353–3367, doi:10.1175/JAS3533.1.

Gettelman, A., and S. C. Sherwood, 2016: Processes responsible for cloud feedback. *Curr. Clim. Change Rep.*, **2**, 179–189, doi:10.1007/s40641-016-0052-8.

Golaz, J. C., M. Salzmann, L. J. Donner, L. W. Horowitz, Y. Ming, and M. Zhao, 2011: Sensitivity of the aerosol indirect effect to subgrid variability in the cloud parameterization of the GFDL atmosphere general circulation model AM3. *J. Climate*, **24**, 3145–3160, doi:10.1175/2010JCLI3945.1.

Gordon, N. D., and S. A. Klein, 2014: Low-cloud optical depth feedback in climate models. *J. Geophys. Res. Atmos.*, **119**, 6052–6065, doi:10.1002/2013JD021052.

Held, I. M., 2005: The gap between simulation and understanding in climate modeling. *Bull. Amer. Meteor. Soc.*, **86**, 1609–1614, doi:10.1175/BAMS-86-11-1609.

Held, I. M., 2014: Simplicity amid complexity. *Science*, **343**, 1206–1207, doi:10.1126/science.1248447.

Held, I. M., and M. J. Suarez, 1994: A proposal for the intercomparison of the dynamical cores of atmospheric general circulation models. *Bull. Amer. Meteor. Soc.*, **75**, 1825–1830, doi:10.1175/1520-0477(1994)075<1825:APFTIO>2.0.CO;2.

Kay, J. E., B. Medeiros, Y.-T. Hwang, A. Gettelman, J. Perket, and M. G. Flanner, 2014: Processes controlling Southern Ocean shortwave climate feedbacks in CESM. *Geophys. Res. Lett.*, **41**, 616–622, doi:10.1002/2013GL058315.

Klein, S. A., and Coauthors, 2009: Intercomparison of model simulations of mixed-phase clouds observed during the ARM Mixed-Phase Arctic Cloud Experiment. I: Single-layer cloud. *Quart. J. Roy. Meteor. Soc.*, **135**, 979–1002, doi:10.1002/qj.416.

Korolev, A., and Coauthors, 2017: Mixed-phase clouds: Progress and challenges. *Meteor. Monogr.*, **58**, 5.1–5.50, doi:10.1175/AMSMONOGRAPHSâĂŘDâĂŘ17âĂŘ0001.1.

Lohmann, U., and D. Neubauer, 2018: The importance of mixed-phase and ice clouds for climate sensitivity in the global aerosol–climate model ECHAM6-HAM2. *Atmos. Chem. Phys.*, **18**, 8807–8828, doi:10.5194/acp-18-8807-2018.

Lohmann, U., and E. Roeckner, 1996: Design and performance of a new cloud microphysics scheme developed for the ECHAM general circulation model. *Climate Dyn.*, **12**, 557–572, doi:10.1007/BF00207939.

McCoy, D. T., P. Field, A. Bodas-Salcedo, G. S. Elsaesser, and M. D. Zelinka, 2020: A regime-oriented approach to observationally constraining extratropical shortwave cloud feedbacks. *J. Climate*, **33**, 9967–9983, doi:10.1175/JCLI-D-19-0987.1.

McCoy, D. T., M. E. Frazer, P. Field, M. D. Zelinka, G. S. Elsaesser, J. Muelmenstaedt, I. Tan, and Z. J. Lebo, 2021: Constraints on moisture convergence-driven extratropical cloud feedback decrease likelihood of very high and very low climate sensitivity. *in prep*.

McCoy, D. T., D. L. Hartmann, and D. P. Grosvenor, 2014: Observed Southern Ocean cloud properties and shortwave reflection. Part I: Calculation of SW flux from observed cloud properties. *J. Climate*, **27**, 8836–8857, doi:10.1175/JCLI-D-14-00287.1.

McCoy, D. T., D. L. Hartmann, and M. D. Zelinka, 2018: Mixed-phase cloud feedbacks. *Mixed-Phase Clouds: Observations and Modeling*, C. Andronache, Ed., Elsevier, 215–236, doi:10.1016/B978-0-12-810549-8.00009-X.

McCoy, D. T., D. L. Hartmann, M. D. Zelinka, P. Ceppi, and D. P. Grosvenor, 2015: Mixed-phase cloud physics and Southern Ocean cloud feedback in climate models. *J. Geophys. Res. Atmos.*, **120**, 9539–9554, doi:10.1002/2015JD023603.

McCoy, D. T., I. Tan, D. L. Hartmann, M. D. Zelinka, and T. Storelvmo, 2016: On the relationships among cloud cover, mixed-phase partitioning, and planetary albedo in GCMs. *J. Adv. Model. Earth Syst.*, **8**, 650–668, doi:10.1002/2015MS000589.

McCoy, D. T., and Coauthors, 2019: Cloud feedbacks in extratropical cyclones: insight from long-term satellite data and high-resolution global simulations. *Atmos. Chem. Phys.*, **19**, 1147–1172, doi:10.5194/acp-19-1147-2019.

Ming, Y., and I. M. Held, 2018: Modeling water vapor and clouds as passive tracers in an idealized GCM. *J. Climate*, **31**, 775–786, doi:10.1175/JCLI-D-16-0812.1.

Mitchell, J., C. Senior, and W. Ingram, 1989: C02 and climate: a missing feedback? *Nature*, **341**, 132–134, doi:10.1038/341132a0.

Morrison, H., and A. Gettelman, 2008: A new two-moment bulk stratiform cloud microphysics scheme in the Community Atmosphere Model, version 3 (CAM3). Part I: Description and numerical tests. *J. Climate*, **21**, 3642–3659, doi:10.1175/2008JCLI2105.1.

Mülmenstädt, J., and Coauthors, 2021: An underestimated negative cloud feedback from cloud lifetime changes. *Nat. Clim. Change*, **11**, 508–513, doi:10.1038/s41558-021-01038-1.

Pierrehumbert, R. T., H. Brogniez, and R. Roca, 2007: On the relative humidity of the atmosphere. *The Global Circulation of the Atmosphere*, T. Schneider, and A. H. Sobel, Eds., Princeton University Press, 143–185.

Pruppacher, H., and J. Klett, 2010: Cloud chemistry. *Microphysics of Clouds and Precipitation, Atmospheric and Oceanographic Sciences Library, vol. 18*, Springer, 237–264, doi:10.1007/978-0-306-48100-0_17.

Rotstayn, L. D., 1997: A physically based scheme for the treatment of stratiform clouds and precipitation in large-scale models. I: Description and evaluation of the microphysical processes. *Q. J. R. Meteorol. Soc.*, **123**, 1227–1282.

Rotstayn, L. D., B. F. Ryan, and J. J. Katzfey, 2000: A scheme for calculation of the liquid fraction in mixed-phase clouds in large-scale models. *Mon. Wea. Rev.*, **128**, 1070–1088.

Senior, C. A., and J. F. B. Mitchell, 1993: Carbon dioxide and climate: The impact of cloud parameterization. *J. Climate*, **6**, 393–418, doi:10.1175/1520-0442(1993)006<0393:CDACTI>2.0.CO;2.

Sherwood, S. C., and Coauthors, 2020: An assessment of Earth's climate sensitivity using multiple lines of evidence. *Reviews of Geophysics*, **58**, e2019RG000 678, doi:10.1029/2019RG000678.

Soden, B. J., and G. A. Vecchi, 2011: The vertical distribution of cloud feedback in coupled ocean-atmosphere models. *Geophys. Res. Lett.*, **38**, L12 704, doi:10.1029/2011GL047632.

Somerville, R. C. J., and L. A. Remer, 1984: Cloud optical thickness feedbacks in the CO2 climate problems. *J. Geophys. Res. Atmos.*, **89**, 9668–9672, doi:10.1029/JD089iD06p09668.

Stephens, G. L., 1978: Radiation profiles in extended water clouds. II. Parameterization schemes. *J. Atmos. Sci.*, **35**, 2123–2132, doi:10.1175/1520-0469(1978)035<2123:RPIEWC>2.0.CO;2.

Storelvmo, T., I. Tan, and A. V. Korolev, 2015: Cloud phase changes induced by CO2 warming–a powerful yet poorly constrained cloud-climate feedback. *Curr. Clim. Change Rep.*, **1**, 288–296, doi:10.1007/s40641-015-0026-2.

Tan, I., L. Oreopoulos, and N. Cho, 2019: The role of thermodynamic phase shifts in cloud optical depth variations with temperature. *Geophys. Res. Lett.*, **46**, 4502–4511, doi:10.1029/2018GL081590.

Tan, I., and T. Storelvmo, 2016: Sensitivity study on the influence of cloud microphysical parameters on mixed-phase cloud thermodynamic phase partitioning in CAM5. *J. Atmos. Sci.*, **73**, 709–728, doi:10.1175/JAS-D-15-0152.1.

Tan, I., and T. Storelvmo, 2019: Evidence of strong contributions from mixed-phase clouds to Arctic climate change. *Geophys. Res. Lett.*, **46**, 2894–2902, doi:10.1029/2018GL081871.

Tan, I., T. Storelvmo, and M. D. Zelinka, 2016: Observational constraints on mixed-phase clouds imply higher climate sensitivity. *Science*, **352**, 224–227, doi:10.1126/science.aad5300.

Tan, I., T. Storelvmo, and M. D. Zelinka, 2018: The climatic impact of thermodynamic phase partitioning in mixed-phase clouds. *Mixed-Phase Clouds: Observations and Modeling*, C. Andronache, Ed., Elsevier, 237–264, doi:10.1016/B978-0-12-810549-8.00010-6.

Terai, C., R. Y. Zhang, S. A. Klein, M. D. Zelinka, J. C. Chiu, and Q. Min, 2019: Mechanisms behind the extratropical stratiform low-cloud optical depth response to temperature in ARM site observations. *J. Geophys. Res. Atmos.*, **124**, 2127–2147, doi:10.1029/2018JD029359.

Terai, C. R., S. A. Klein, and M. D. Zelinka, 2016: Constraining the low-cloud optical depth feedback at middle and high latitudes using satellite observations. *J. Geophys. Res. Atmos.*, **121**, 9696–9716, doi:10.1002/2016JD025233.

Tselioudis, G. W., B. Rossow, and D. Rind, 1992: Global patterns of cloud optical thickness variation with temperature. *J. Climate*, **5**, doi:0.1175/1520-0442(1992)005<1484:GPOCOT>2.0.CO;2.

Vial, J., J.-L. Dufresne, and S. Bony, 2013: On the interpretation of inter-model spread in CMIP5 climate sensitivity estimates. *Climate Dyn.*, **41**, 3339–3362, doi:10.1007/s00382-013-1725-9.

Wall, C. J., and D. L. Hartmann, 2015: On the influence of poleward jet shift on shortwave cloud feedback in global climate models. *J. Adv. Model. Earth Syst.*, **7**, doi:10.1002/2015MS000520.

Zelinka, M. D., T. A. Myers, D. T. McCoy, S. Po-Chedley, P. M. Caldwell, P. Ceppi, S. A. Klein, and K. E. Taylor, 2020: Causes of higher climate sensitivity in CMIP6 models. *Geophys. Res. Lett.*, **47**, e2019GL085 782, doi:10.1029/2019GL085782.

Zelinka, M. D., C. Zhou, and S. A. Klein, 2016: Insights from a refined decomposition of cloud feedbacks. *Geophys. Res. Lett.*, **43**, 9259–9269, doi:10.1002/2016GL069917.

Zhao, M., 2014: An investigation of the connections among convection, clouds, and climate sensitivity in a global climate model. *J. Climate*, **27**, 1845–1862, doi:10.1175/JCLI-D-13-00145.1.

# LIST OF TABLES

TABLE 1. Description of the experiments.

| Name(s) | Perturbation(s) |
|---|---|
| Ctrl | the control with $RH_c$ = 83.3% |
| Tse2K | 2-K warming applied to the *t*emperature seen by the (*s*tratiform) cloud scheme and surface *e*vaporation |
| | Process-level Experiments (Section 3a) |
| Qse2K | 2-K warming applied to calculation of $q_s$ for the cloud scheme and surface *e*vaporation |
| MI2K | 2-K warming applied to *mi*crophysical processes: BF process, melting, homogeneous freezing, and initial phase partitioning |
| BF2K | 2-K warming applied to the *BF* process |
| ME2K | 2-K warming applied to *me*lting |
| | Perturbed Parameter Experiments (Section 3b) |
| {quar, halv, doub, quad}BF | the BF conversion rate multiplied by {0.25, 0.5, 2, 4} |
| rh{767, 800, 867, 900} | $RH_c$ = {76.7%, 80%, 86.7%, 90%} |
| v{050, 075, 125, 150} | the ice fall speed multiplied by {0.5, 0.75, 1.25, 1.5} |
| {name}_Tse2K | the corresponding Tse2K experiment for {name} (e.g., quarBF_Tse2K) |

740 TABLE 2. Normalized changes in LWP and IWP (g $m^{-2}$ $K^{-1}$) in the process-level experiments. The normalized
741 fractional changes (% $K^{-1}$) are in parentheses. The climatological values (g $m^{-2}$) in Ctrl are also given.

| | Extratropics | | Mid-Latitudes | | High-Latitudes | |
|---|---|---|---|---|---|---|
| | LWP | IWP | LWP | IWP | LWP | IWP |
| Ctrl | 29.9 | 35.6 | 38.3 | 42.7 | 4.6 | 14.1 |
| Tse2K | 3.0 (9.9) | 0.9 (2.4) | 3.6 (9.3) | 0.8 (1.9) | 1.1 (24.2) | 1.0 (7.2) |
| Qse2K | 0.5 (1.7) | 2.4 (6.8) | 0.6 (1.6) | 2.8 (6.7) | 0.2 (5.2) | 1.1 (7.9) |
| MI2K | 2.2 (7.4) | -1.4 (-4.0) | 2.6 (6.9) | -1.9 (-4.4) | 0.9 (19.4) | 0.0 (-0.3) |
| BF2K | 1.7 (5.5) | -0.1 (-0.2) | 1.9 (5.0) | -0.1 (-0.2) | 0.9 (18.7) | 0.0 (0.2) |
| ME2K | 0.6 (2.1) | -1.4 (-3.9) | 0.8 (2.1) | -1.8 (-4.2) | 0.0 (0.8) | -0.1 (-0.5) |

# LIST OF FIGURES

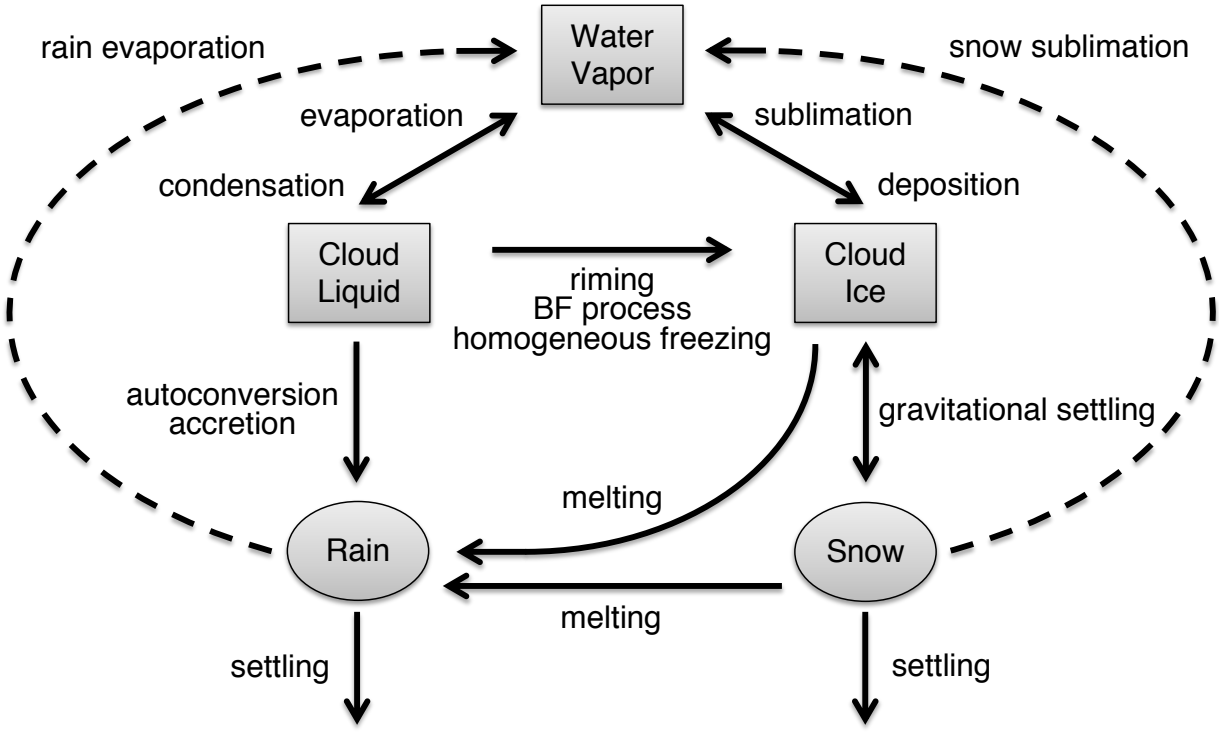


776 FIG. 1. Schematic of tracers and processes in the cloud microphysics scheme. Quantities in rectangles are
777 prognostic tracers, and those in ovals are diagnostic variables.

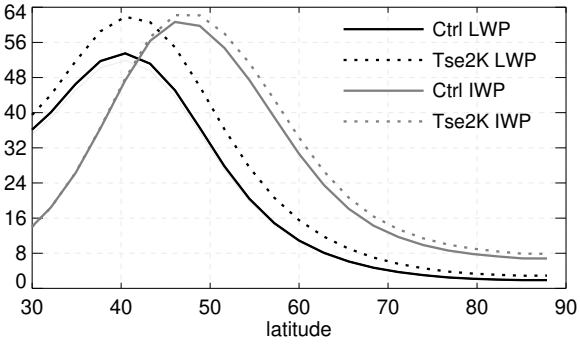


778 FIG. 2. Zonal-mean LWP and IWP (g $m^{-2}$) in Ctrl and Tse2K experiments, averaged between hemispheres as
779 for all following figures.

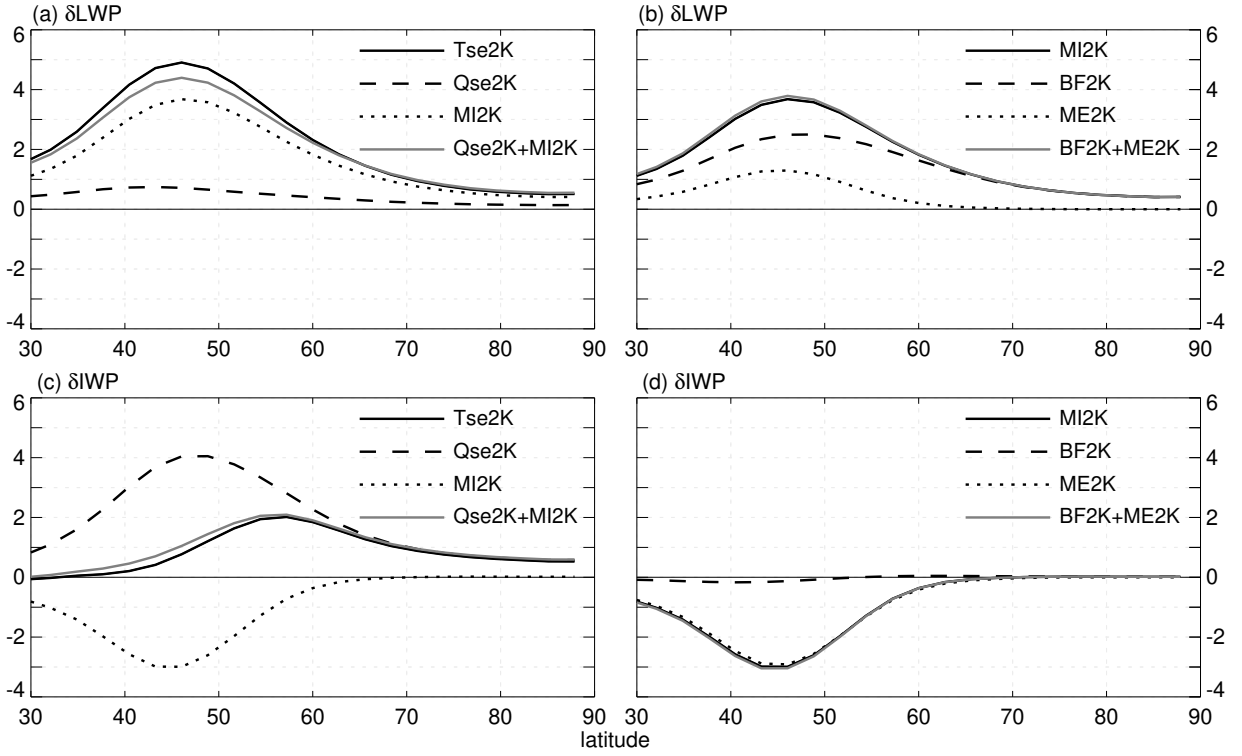


780 FIG. 3. Normalized changes in the zonal-mean extratropical LWP (the upper panels) and IWP (the lower
781 panels) (g $m^{-2}$ $K^{-1}$) in the process-level experiments.

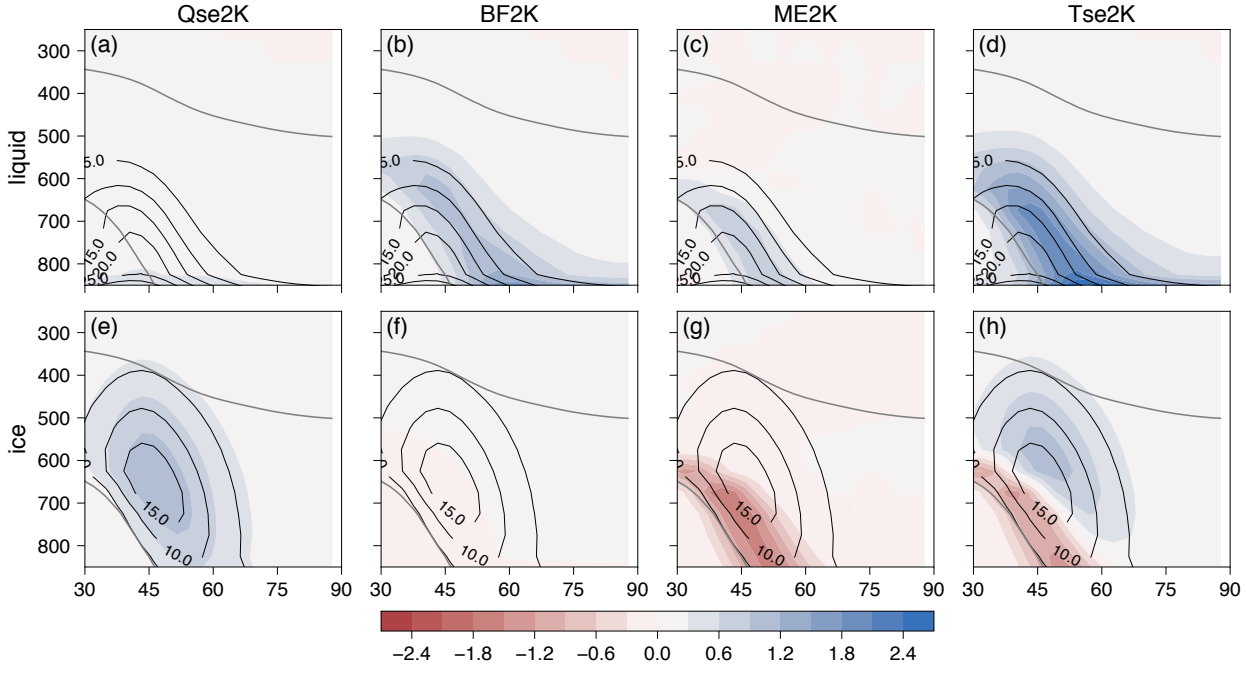


FIG. 4. Vertical distributions of the normalized changes in the zonal-mean mixing ratios of cloud liquid and ice ($10^{-6}$ kg kg$^{-1}$ K$^{-1}$) in the key process-level experiments. Differences between the perturbation and Ctrl runs are shown as colored shading. Ctrl run values are depicted by the contours with a spacing of 5 $10^{-6}$ kg kg$^{-1}$. Thick grey lines show the 0°C and -40°C isotherms. The x- and y-axes are latitude and pressure (hPa), respectively.

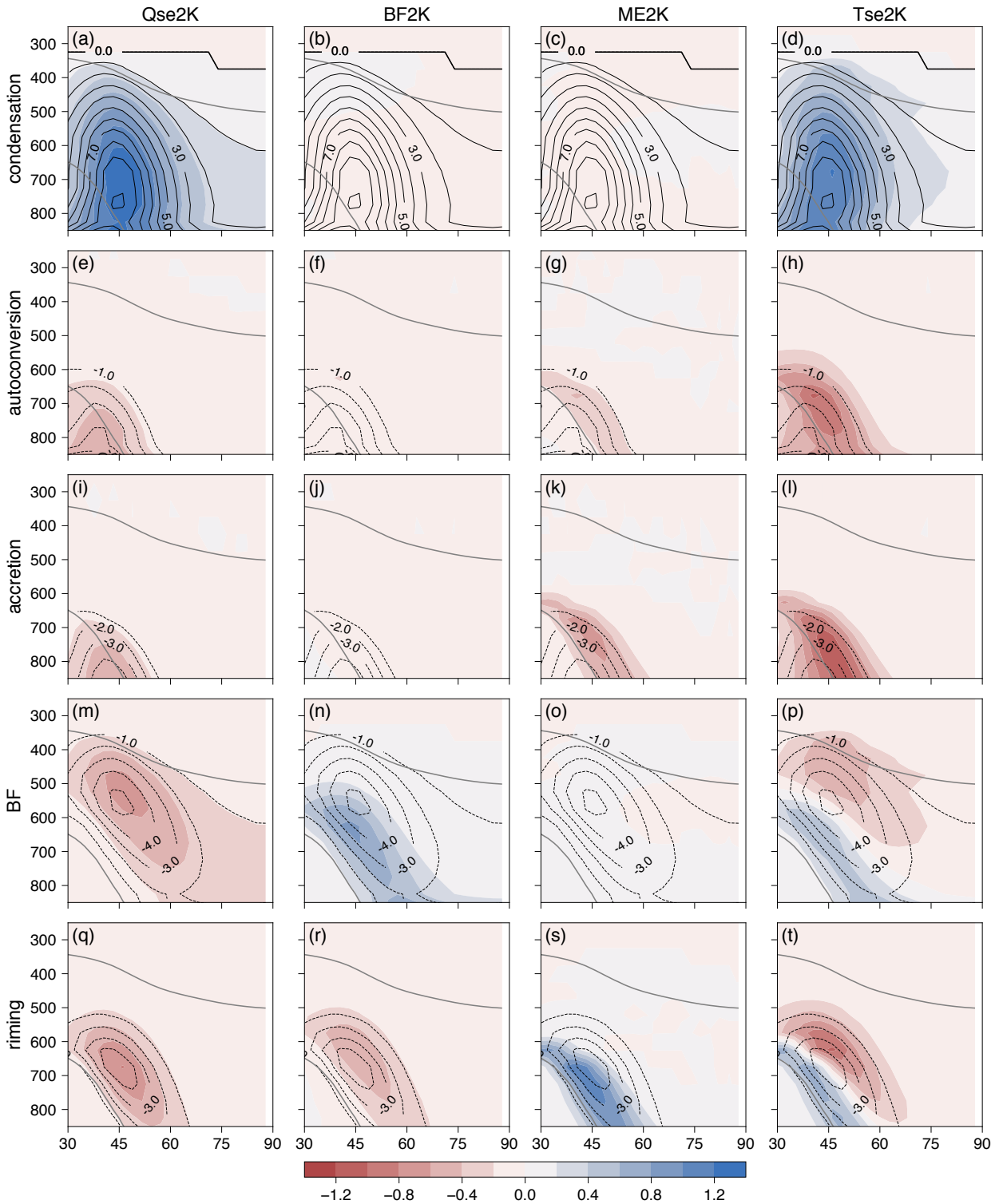


786 FIG. 5. Vertical distributions of the normalized changes in the zonal-mean time tendency terms of cloud liquid
787 mixing ratio ($10^{-9}$ kg kg$^{-1}$ s$^{-1}$ K$^{-1}$) in the key process-level experiments. Differences between the perturbation
788 and Ctrl runs are shown as colored shading where a positive value indicates an increase in cloud liquid tendency.
789 Ctrl run values are represented by the contours with a spacing of 1 $10^{-9}$ kg kg$^{-1}$ s$^{-1}$. The tendency terms shown
790 are condensation, autoconversion, accretion, the BF process, and riming. Thick grey lines are the 0°C and -40°C
791 isotherms. The x- and y-axes are latitude and pressure (hPa), respectively.

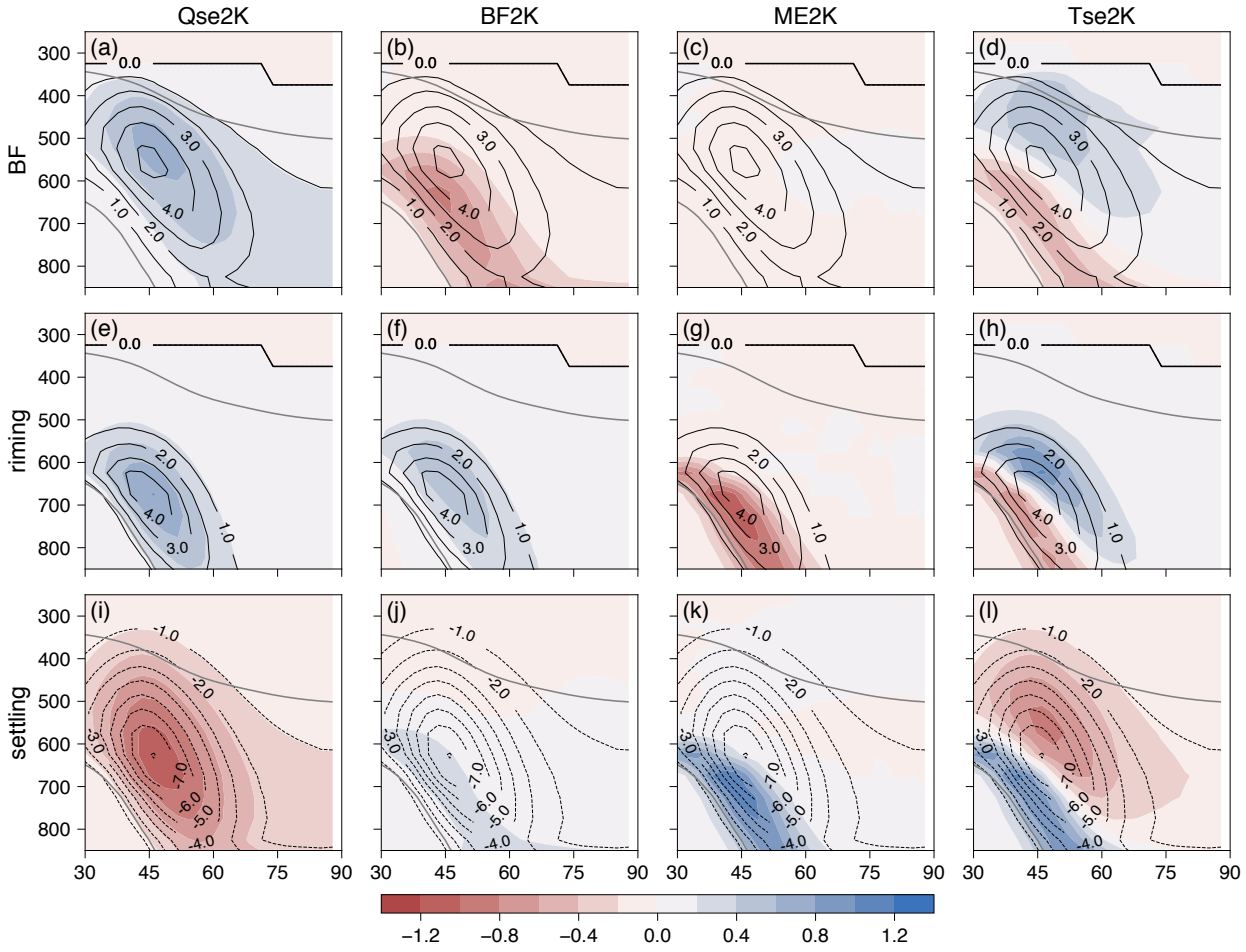


792 FIG. 6. As Fig. 5, but for cloud ice instead of cloud liquid, with tendency terms shown being the BF process,
793 riming, and gravitational ice settling.

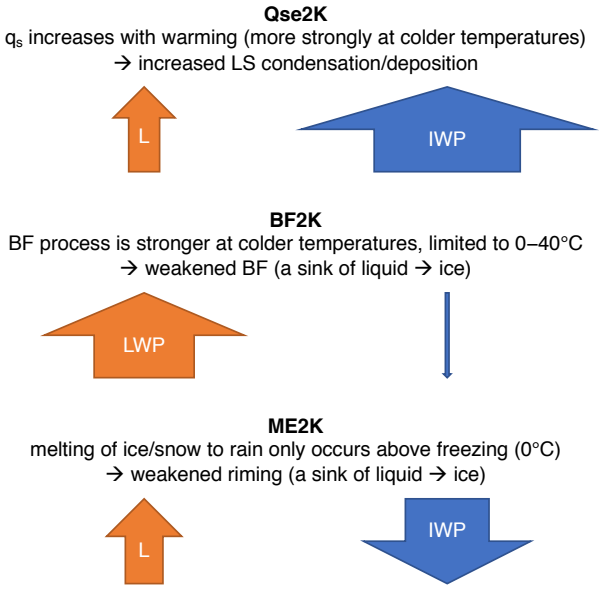


794 FIG. 7. Summary of the three main processes (highlighted by Qse2K, BF2K, and ME2K experiments)
795 underlying the LWP/IWP feedback. Arrow width and direction represent the relative magnitude and sign
796 (upward denoting an increase) of the LWP/IWP changes, respectively.

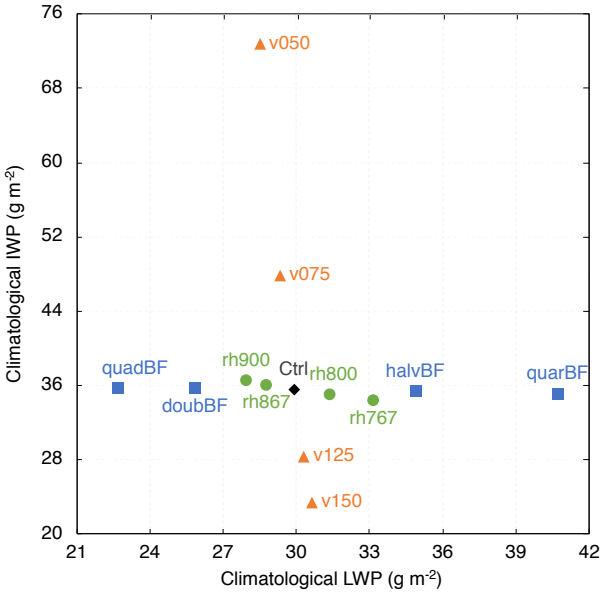


797 FIG. 8. Climatological LWP (g $m^{-2}$) plotted against the climatological IWP (g $m^{-2}$) in the perturbed parameter
798 experiments.

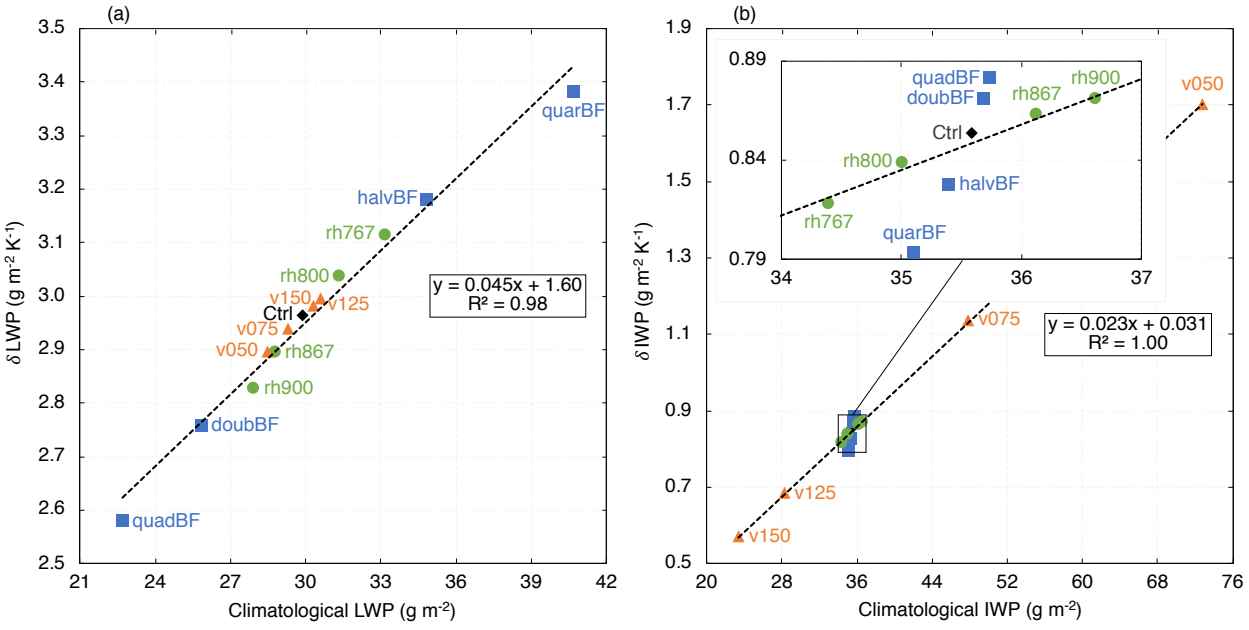


FIG. 9. Normalized changes in LWP/IWP (g m$^{-2}$ K$^{-1}$) in the full warming (Tse2K) experiments plotted against the climatological LWP/IWP (g m$^{-2}$) in the perturbed parameter experiments. Panels (a) and (b) are for LWP and IWP, respectively. The rectangle in Panel (b) is a blowup of the data points clustered around Ctrl.

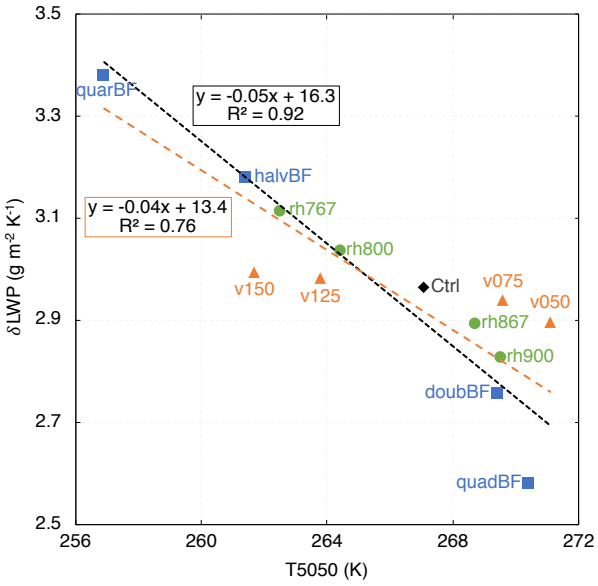


802 FIG. 10. Normalized changes in LWP (g $m^{-2}$ $K^{-1}$) in the full warming (Tse2K) experiments plotted against
803 the climatological T5050 in the perturbed parameter experiments. The black and orange dotted lines represent
804 the best linear fits without and with the ice fall speed experiments, respectively.